ADVANCED MATERIALS
www.advmat.de

Giant Blue Energy Harvesting in Two-Dimensional Polymer Membranes with Spatially Aligned Charges

Xiaohui Liu, Xiaodong Li, Xingyuan Chu, Bowen Zhang, Jiaxu Zhang, Mike Hambsch, Stefan C. B. Mannsfeld, Mino Borrelli, Markus Löffler, Darius Pohl, Yuanwu Liu, Zhen Zhang, and Xinliang Feng**

Blue energy between seawater and river water is attracting increasing interest, as one of the sustainable and renewable energy resources that can be harvested from water. Within the reverse electrodialysis applied in blue energy conversion, novel membranes with nanoscale confinement that function as selective ion transport mediums are currently in high demand for realizing higher power density. The primary challenge lies in constructing well-defined nanochannels that allow for low-energy barrier transport. This work proposes a concept for nanofluidic channels with a simultaneous dual electrostatic effect that can enhance both ion selectivity and flux. To actualize this, this work has synthesized propidium iodide-based two-dimensional polymer (PI-2DP) membranes possessing both skeleton charge and intrinsic space charge, which are spatially aligned along the ion transport pathway. The dual charge design of PI-2DP significantly enhances the electrostatic interaction between the translocating anions and the cationic polymer framework, and a high anion selectivity coefficient (≈0.8) is reached. When mixing standard artificial seawater and river water, this work achieves a considerable power density of 48.4 W m^{-2}, outperforming most state-of-the-art nanofluidic membranes. Moreover, when applied between the Mediterranean Sea and the Elbe River, an output power density of 42.2 W m^{-2} is achieved by the PI-2DP. This nanofluidic membrane design with dual-layer charges will inspire more innovative development of ion-selective channels for blue energy conversion that will contribute to global energy consumption.

1. Introduction

Water, a ubiquitous and essential element on our planet, holds immense potential as a source of energy in various forms, such as hydropower, tidal energy, and blue energy. Among these renewable and sustainable energy resources, blue energy derived from the encounter of oceans and rivers shows significant promise due to its daily constancy compared to others.[1] Reverse electrodialysis is the main technology to harvest and convert the Gibbs free energy available in a salinity gradient into electrical power, in which the ion-exchange membrane is a fundamental component.[2,3] However, traditional membranes such as commercial ion-exchange membranes are hindered by their high ion transport resistance, which results in low power densities of less than 2 W m^{-2}.[4–6] Therefore, developing novel membranes with nanoscale confinement serving as a selective ion transport medium is crucial.[7] Towards this end, single nanofluidic channels with high power densities have been explored through complicated fabrications, such as single boron nitride nanotubes and single-layer MoS_2

X. Liu, X. Chu, J. Zhang, M. Borrelli, X. Feng
Center for Advancing Electronics Dresden (cfaed) and Faculty of Chemistry and Food Chemistry
Technische Universität Dresden
01062 Dresden, Germany
E-mail: xinliang.feng@tu-dresden.de

X. Li
Max Planck Institute of Microstructure Physics
06120 Halle (Saale), Germany

B. Zhang
Fraunhofer Institute for Ceramic Technologies and Systems (IKTS)
Maria-Reiche-Strasse 2
01109 Dresden, Germany

M. Hambsch, S. C. B. Mannsfeld
Center for Advancing Electronics Dresden (cfaed) and Faculty of Electrical and Computer Engineering Technische Universität Dresden
01062 Dresden, Germany

M. Löffler, D. Pohl
Dresden Center for Nanoanalysis
Center for Advancing Electronics Dresden
Technische Universität Dresden
01062 Dresden, Germany

Y. Liu
Physical Chemistry
Technische Universität Dresden
Zellescher Weg 19, 01069 Dresden, Germany

The ORCID identification number(s) for the author(s) of this article can be found under https://doi.org/10.1002/adma.202310791

DOI: 10.1002/adma.202310791

membranes with drilled pores.[8–10] Recently, two-dimensional (2D) membranes that can be facilely integrated with nanofluidic channels are becoming promising candidates, such as restacked exfoliated graphene and transition metal carbide/nitride nanosheets that use the interplanar spacings and interstitial gaps as ion transport channels.[11–19] To date, the major challenge is to construct well-defined nanochannels that allow for low-energy barrier transport under the water salinity gradients. In general, ion transport relies strictly on the collective interaction of confined charges with the mobile ions, and thus the charge distribution inside the membrane channels plays a decisive role. The post-introducing spatial charge can slightly increase the charge density of 2D restacked membranes, but it fails to effectively alleviate the ion transport barrier posed by their tortuous long channels.[15] As a result, the achieved power densities remain limited for the state-of-the-art 2D membranes (less than 10 W m^{-2}).

In this study, we unveil a confined simultaneous dual electrostatic effect within ultrathin 2D polymer (2DP) membranes, characterized by precisely defined ion transport channels, which can significantly augment both ion selectivity and flux, leading to a marked enhancement in the overall osmotic power output. Building upon this foundation based on the theoretical design of dual electrostatic effect (**Figure 1**a), we successfully synthesized two types of fully crystalline cationic 2DP membranes using the on-water surface chemistry: ethidium bromide-based 2DP (EB-2DP) possessing only skeleton charges, and propidium iodide-based 2DP (PI-2DP) possessing both skeleton charge and intrinsic space charge. The PI-2DP membrane with a pore size of ≈1.8 nm, synthesized from PI monomer with a double unit positive charge, possesses intrinsic space charges that are spatially aligned, which could couple with the inherent skeleton charges, synergistically enhancing the anion (Cl^-, Br^-, I^-) transport. Specifically, the PI-2DP achieves an ultrahigh osmotic current (I_{os}) of 4.8 kA m^{-2}, surpassing 2.3 kA m^{-2} of the contrasting EB-2DP. Moreover, the anion selectivity coefficient of PI-2DP is nearly twice that of EB-2DP, indicating a low-energy barrier within its nanochannels. When employed in harvesting the osmotic energy between artificial seawater and river water, the PI-2DP membranes deliver a maximum power density of 48.4 W m^{-2}. When the testing area is reduced to a sub-micrometre scale (<1 μm^2), a record value of 259 W m^{-2} is achieved, outperforming the state-of-the-art nanofluidic membranes. In a real-world application scenario, combining water from the Mediterranean Sea and the Elbe River yields an exceptionally high blue power of 42.2 W m^{-2}. This innovative PI-2DP membrane promises to inspire advanced ion-exchange membranes and accelerate the harnessing of blue energy from the abundant water resources in the world's vast oceans and rivers.

Z. Zhang
School of Chemistry and Materials Science
University of Science and Technology of China
Hefei 230026, China
E-mail: zhenzhang@ustc.edu.cn
Z. Zhang
Suzhou Institute for Advanced Research
University of Science and Technology of China
Suzhou 215123, China

2. Results

2.1. Guided Theoretical Design

We first design the dual electrostatic effect in pore channels based on numerical simulations using the Poisson and Nernst–Planck (PNP) equations.[20] As demonstrated in Figure 1a, three types of models are constructed to simulate the inherent nanochannels: models (i) and (ii) simulate the nanochannels having one positive charge layer of 1.2 and 1.8 nm diameters, respectively; model (iii) simulates the nanochannel which has both inner (d = 1.2 nm) and outer (d = 1.8 nm) positively charged layers. The cross-section three-dimensional (3D) anion concentration profiles corresponding to the simulated models under a concentration gradient are demonstrated on each model's right side. It is clear that the concentration of anions increases closer to the channel wall due to the attraction from charged sites. Compared to model (ii), model (i) has a higher anion concentration, which is attributed to the more overlapping area of the electric double layer (EDL) in its narrower charged channel. The anion concentration is even higher inside model (iii), indicating its superior ion-selective transport due to the existence of another charged layer. We then plotted the ion concentration along both the radial and axial directions (Figure S1, Supporting Information). Along the radial direction, the closer to the positively charged sites in the nanochannel wall, the higher the concentration of anions and the lower the concentration of cations. Model (iii) has the topmost anion concentration and the least cation concentration compared to the other two channel models, both in radial and axial directions benefiting from its dense charge distribution along the channel, suggesting the most efficient charge separation effect. The calculated electric potential shows the same trend with the anion concentration along the radial direction (Figure 1b), exhibiting a sub-peak in the position of the second charge layer. The coupled PNP model allows us to calculate the exact value of the osmotic current (I_{os}) and osmotic voltage (V_{os}) as demonstrated in Figure 1c. The much higher V_{os} and I_{os} of the model (iii) indicates the considerable effects of the inner charged layer on the osmotic conversion process. As a result, model (iii) yields an osmotic power density of 7.3 W m^{-1}, which is 16% higher than the sum (6.3 W m^{-1}) of model (i) and (ii) (Figure 1d).

2.2. Fully Crystalline 2DP Membranes

According to the charge distribution and channel structure in the above numerical model (ii) and (iii), we thus designed two types of cationic 2DPs as shown in **Figure 2**a,b, which are ethidium bromide-based 2DP (EB-2DP) and propidium iodide-based 2DP (PI-2DP), respectively. PI-2DP possesses both spatially aligned skeleton charge and space charge along the nanochannel, while EB-2DP has only skeleton charge. To investigate the effects of the spatially aligned charge on the selective ion transport, we also choose another monomer, 3,8-diamino-6-phenylphenanthridine (DP) as **M1** (monomer 1) to synthesize DP-2DP that has a similar backbone structure but without charged sites. As illustrated in Figure S2 (Supporting Information), the continuous 2DP membranes are synthesized via the Schiff-base 2D polycondensation between **M1** (PI, EB, DP) and **M2** (monomer 2) (1,3,5-triformylphloroglucinol (TFP), and

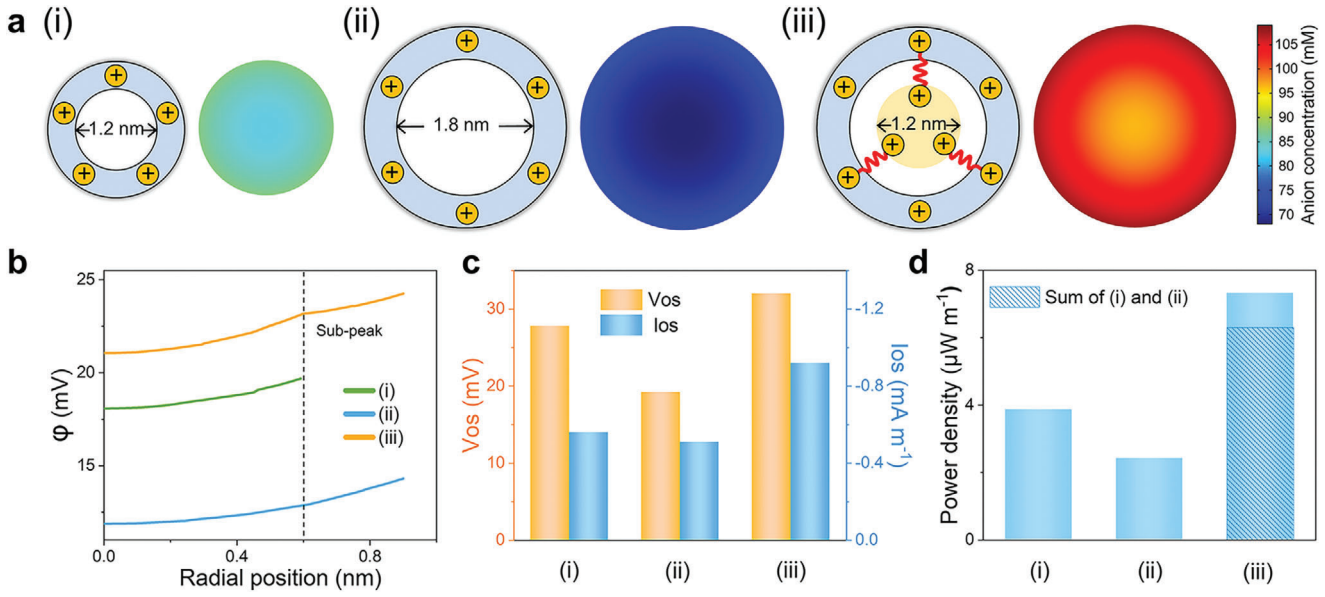

Figure 1. A model design for the high-performance nanofluidic channel. a) Numerical simulation models of 1D nanochannels and anion concentration profiles obtained from models (i), (ii), and (iii), respectively. Model (i) and (ii) simulate the nanochannels that have one charged layer of 1.2 and 1.8 nm diameters, respectively; model (iii) simulates the nanochannel which has both inner (d = 1.2 nm) and outer (d = 1.8 nm) charged layers. b) Variation of potential along the radial directions of three models. c,d) Simulated V_{os} and I_{os} (c), and power density (d) of the three models.

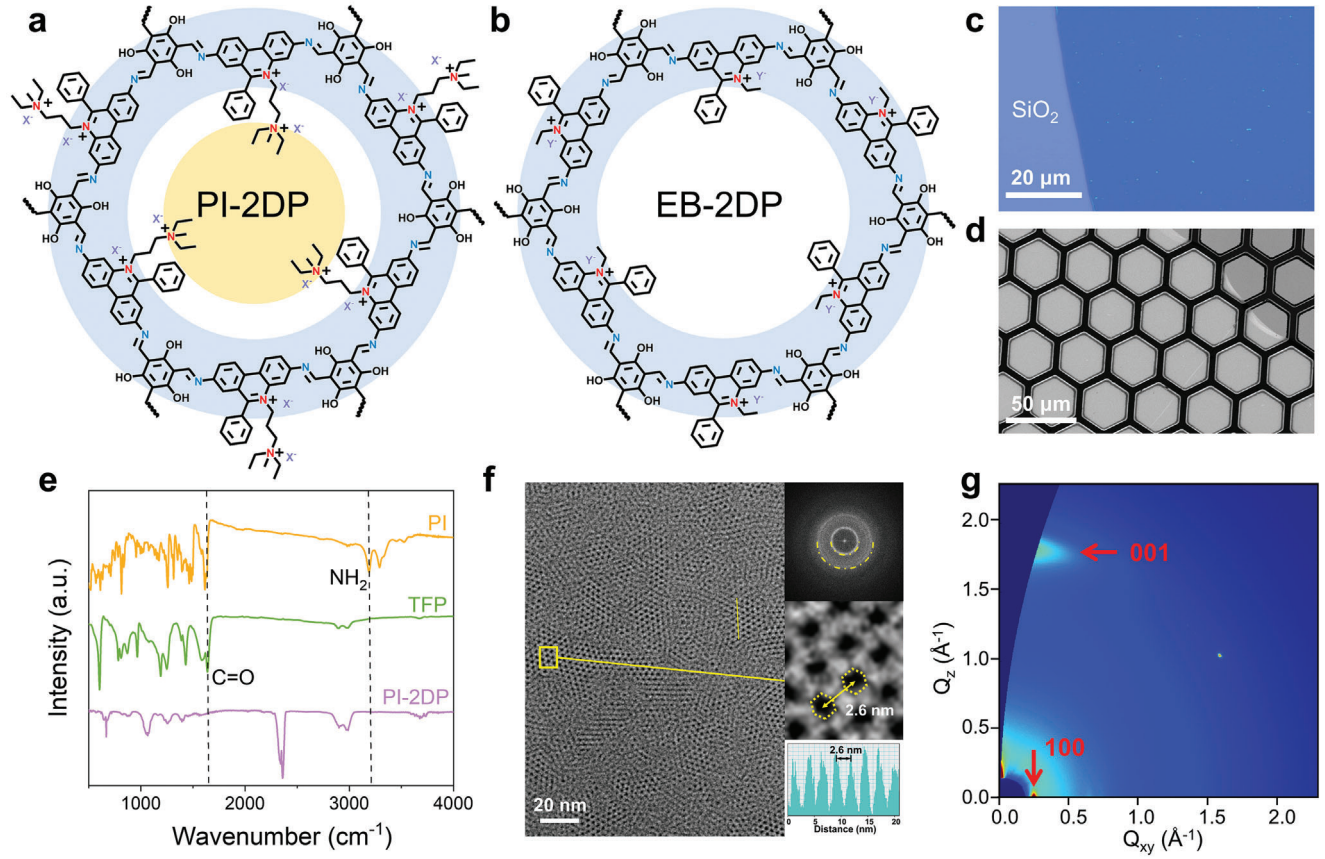

Figure 2. Design and characterization of 2DPs. a,b) Schematics of PI-2DP (a) and EB-2DP (b) designed based on model (iii) and model (ii); X^- represents $CF_3SO_3^-$ and Y^- represents Cl^-. c,d) Optical microscopy image (c) and SEM image (d) of synthesized PI-2DP membrane. e) FTIR spectra of monomers and synthesized PI-2DP membrane. f) HRTEM image and SAED (top inset) of the synthesized PI-2DP. Middle inset: magnified HRTEM image of PI-2DP. Bottom inset: Intensity profiles along the yellow line. g) GIWAXS image of PI-2DP membrane.

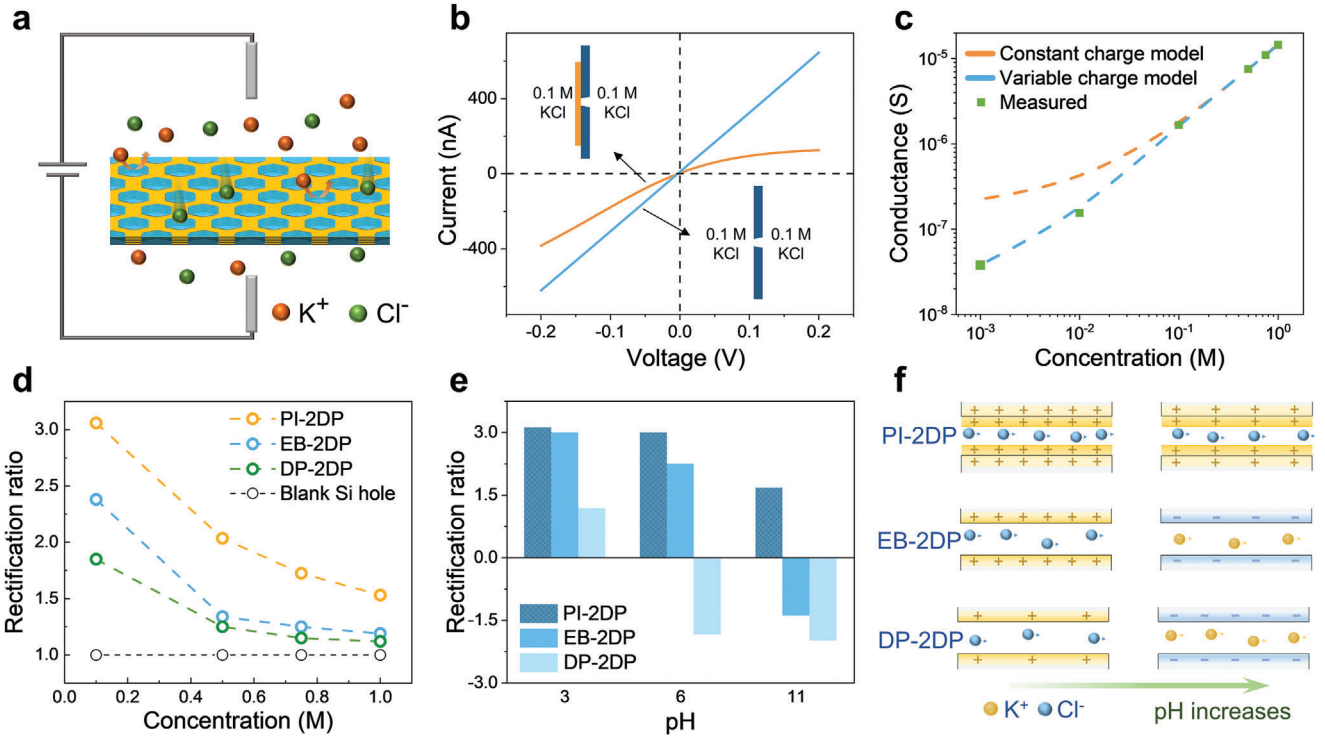

Figure 3. Charge-governed transmembrane ion transport. a) Schematic illustration of the experimental setup for measuring the ionic transport across the PI-2DP membrane. b) *I–V* curves of the PI-2DP membrane and blank Si hole measured in 0.1 M KCl electrolyte solution. c) The ionic conductance of PI-2DP under a series of KCl solution concentrations. The constant charge model assumes the surface charge as 3.45 mC m^{-2}. d,e) Rectification ratio of PI−, EB−, and DP-2DP membranes under various KCl concentrations (d) and as a function of pH values in 0.1 M KCl solutions (e). f) Illustration of the selective ion transport inside the PI−, EB, and DP-2DP channel with different pH values of KCl solutions.

the surfactant-monolayer-assisted interfacial synthesis (SMAIS) method is employed (Figure S3, Supporting Information).[21,22] The resultant 2DP membranes from the on-water surface were then transferred onto various substrates for subsequent characterizations. Under optical microscopy, the 2DP membranes with homogeneous morphologies were visualized (Figure 2c and Figure S4, Supporting Information). The thickness of three thin 2DP membranes is in the range of 12–14 nm according to the atomic force microscopy (AFM) studies (Figure S5, Supporting Information). In addition, all these three 2DPs can suspend over large holes on a copper grid, suggesting excellent mechanical stability (Figure 2d and Figure S6, Supporting Information). The successful formation of PI−, EB−, and DP-2DPs is further confirmed by the lack of the amino peak at 3190 cm^{-1} of M1 and aldehyde peak at 1642 cm^{-1} of M2 in the Fourier transform infrared (FTIR) spectra (Figure 2e and Figure S7, Supporting Information). The constituent elements in the membranes are characterized by the X-ray photoelectron spectroscopy (XPS) analysis (Figure S8, Supporting Information). Then the crystallinity and lattice structure of 2DPs were characterized by selected-area electron diffraction (SAED) and high-resolution transmission electron microscopy (HRTEM) imaging (Figure 2f and Figure S9, Supporting Information), which demonstrate that the fully crystalline 2DPs with crystal domain sizes of 10–70 nm were obtained. The diffraction rings in the SAED pattern also indicate the polycrystalline nature of these three 2DP membranes (inset of Figure 2f, and Figure S9, Supporting Information, insets). The nearest reflection at 0.38 nm^{-1} corresponds to the interplanar spacing of 2.6 nm. Synchrotron grazing incidence wide-angle X-ray scattering (GIWAXS) analysis was used to study the crystallinity of 2DPs on the macroscopic scale (Figure 2g and Figure S10, Supporting Information). The resultant unit cell is assigned with $a = b = 3.0$ nm, which agrees well with the lattice structure derived from DFT calculation (Figure S11, Table S1, Supporting Information) and SAED pattern. The in-plane peaks at $Q_{xy} = 0.25$ $Å^{-1}$ of PI− and EB-2DP correspond to the 100 Bragg reflections of a hexagonal lattice. A diffuse arc at $Q_z = 1.82$, 1.85, and 1.89 $Å^{-1}$of PI−, EB−, and DP-2DP in the out-of-plane direction reveals the face-on orientation of 2D polymer layers with a π–π stacking distance of 0.35, 0.34, and 0.33 nm of PI−, EB−, and DP-2DP, respectively.

2.3. Transmembrane Ion Transport

The achieved PI-2DP membranes have intrinsic nanochannels with positively charged sites that would attract counter-ions to form an EDL. Especially, when the channel size is comparable to the Debye length, the EDL would overlap, which would transport the counter-ions (Cl^-) more effectively, while rejecting the co-ions (K^+) (**Figure 3a**). To experimentally evaluate the transmembrane ion transport behavior, we transferred the cationic 2DP on a silicon wafer which has an open hole of about 12 μm^2. The PI-2DP membrane exhibits ionic rectification

behavior, evidenced by a nonlinear current–voltage (*I–V*) curve, which is totally different from the linear *I–V* curve of the blank Si hole (Figure 3b and Figure S13, Supporting Information).[23,24] In the plot of the conductance of PI-2DP against the concentration, the conductance deviates from the linear bulk behavior at low concentration, and decreases much more slowly as the concentration decreases (Figure 3c). This result reveals that PI-2DP is enabled with charge-governed behavior in the transmembrane ionic transport, which can be ascribed to its inherent charge.[25] By fitting the conductance–concentration data (Section 4.2), we obtained the surface charge density of about +3.45 mC m^{-2} for PI-2DP at 0.1 M KCl, which is higher than other reported 2D materials such as black phosphorus, graphene oxide, and boron nitride nanosheets (0.2–2 mC m^{-2}).[26–29] Both the EB- and DP-2DP membranes also exhibit ionic rectification behavior (Figure S14, Supporting Information), implying that they all exhibit net surface charge in the electrolyte solution. The zeta potential of the PI−, EB−, and DP-2DP membranes was measured which are 32.4, 14.2, and −9.1 mV, respectively, indicating the strong positive charge property and great potential of the PI-2DP in osmotic energy conversion (Figure S15, Supporting Information). The ionic diode property of the three 2DP membranes can be quantified by the rectification ratio, which is calculated as the ratio of current at a negative potential (−0.2 V) and positive potential (0.2 V) (Figure 3d).[30] PI-2DP membranes with spatially aligned charges in the channels have more effective ion transport ability which leads to a much higher rectification ratio than that of EB− and DP-2DP at every concentration of KCl electrolyte. At 0.1 M KCl, PI-2DP reaches a high rectification ratio of 3.1, when that of EB-2DP and DP-2DP are only 2.4 and 1.9. It is worth noting that the rectification ratio of all the 2DPs decreases with the increasing KCl concentration, which is due to the thinner EDL at the higher concentration.[31]

We also found that PI-2DP membrane exhibits more consistent selectivity toward Cl^- ion than EB−and DP-2DP under different pH conditions (blank Si hole shows nonselectivity, Figure S16, Supporting Information), as judged from PI-2DP's consistent positive rectification ratio in the pH range 3 to 11 (Figure 3e). The measured zeta potential of PI-2DP also keeps positive in this pH range, confirming the stable positive charged property of the PI-2DP membrane (Figure S17, Supporting Information). At pH 3, they all demonstrate anion selectivity (rectification ratios are +3.1, +3.0, and +1.2 for PI-, EB-, and DP-2DP, respectively) that can be ascribed to the positively charged sites already existing in the PI− and EB-2DP structure, as well as the protonated phenanthrene N and imine N in all three 2DP membranes (Figure 3f). As pH increases from 3 to 11, the hydroxyl groups in the skeletons of these three 2DPs would be deprotonated to a large degree. PI-2DP shows stable anion selectivity in this pH range (rectification ratio from +3.1 to +1.7) due to the large population of cationic sites existing in the PI-2DP's channel which counteracts the effect from the deprotonated hydroxyl groups. In contrast, EB-2DP and DP-2DP change their selective ion type from anion to cation at pH 9.1 and 3.4, respectively (Figure S14, Supporting Information). Because EB− and DP-2DP lack positively charged sites in the backbone structures, their selectivity is driven by the deprotonated hydroxyl groups. Thereby, the stable anion selectivity of PI-2DP enables its high promising potential in transmembrane ion transport.

2.4. Osmotic Energy Conversion

To quantitively demonstrate the influence of charge population on the selective ion transport process, we applied a range of KCl concentration gradients on the two sides of the 2DP membranes (**Figure 4a**). The 2DP membranes can selectively transport K^+ or Cl^- depending on their charge polarity, then the net osmotic potential difference (V_{os}) and I_{os} are generated (Figure 4b and Figure S18 , Supporting Information), which can be directly recorded from the intercepts of the *I–V* curves, respectively. As shown in Figure 4c and Figure S19a (Supporting Information), the V_{os} of PI-2DP and EB-2DP membranes is both positive, indicating a preferential selectivity toward anions, but with the values of PI-2DP (+49.4 mV) much higher than that of EB-2DP (+22.3 mV) at 25-fold KCl. In contrast, the negative V_{os} of the DP-2DP membrane shows its selective cation diffusion behavior. The corresponding ion selectivity can be quantified by the selectivity coefficient, $S = V_{os}F/RT\Delta \ln C$[32,33] As shown in Figure 4d, *S* of PI-2DP is much higher than that of EB- and DP-2DP in all concentration gradients, approaching ≈0.8 at a 10-fold, which demonstrates the considerable impact of dual charge sites distributing along the PI-2DP channel. Moreover, lower *S* was observed for all three 2DPs in the high-concentration region, which is because the increased concentration leads to thinner EDL, and hence lower ion selectivity (Figure 4d, inset). The calculated transference number $t_- = (S + 1)/2$ of these three membranes has the same trend with selectivity coefficient (Figure S20, Supporting Information). For all three 2DPs, the current increases with the rise of the concentration gradient since I_{os} is driven by the concentration gradient (Figure 4e and Figure S19b, Supporting Information). Similar to the case of V_{os}, PI-2DP also exhibits the highest I_{os} (−58 nA) compared with EB-2DP (−26.7 nA) and DP-2DP (+22.5 nA), about 120% and 160% higher at 100-fold concentration gradient, respectively. The osmotic energy conversion performance can be evaluated by the theoretical power output, $P_{max} = I_{os} \times V_{os}/4A$ (Figure 4f). Due to the higher I_{os} and V_{os}, PI-2DP can achieve a maximum P_{max} of 40.4 W m^{-2} at 50-fold KCl, surpassing EB− and DP-2DP by more than 300%. Next, the salinity gradient between the standard artificial seawater (0.5 M NaCl) and river water (0.01 M NaCl) was applied to evaluate the actual working performance. The P_{max} of PI-2DP membrane reaches 46.8 W m^{-2}, higher than that under 50-fold KCl (40.4 W m^{-2}) (Figure S21, Supporting Information), which can be ascribed to the lower diffusion coefficient of Na^+ ions (1.33×10^{-9} m^2 s^{-1}) versus K^+ ions (1.96×10^{-9} m^2 s^{-1}).[34] In the case of NaCl, the Cl^- diffuses faster, contributing to more efficient charge separation.[35] The influence of the PI-2DP membrane thickness on the performance is also investigated as shown in Figure S22 (Supporting Information). The enough thickness can enable sufficient functional groups in the membrane, achieving an optimal ion selective functionality. Consequently, this realizes enhanced anion selectivity and enlarged anion flux. However, further increase in thickness causes larger resistance, leading to a subsequent decrease in I_{os}.

The harvested osmotic power can be exported by applying an external load resistance, and the output power density is calculated as $P_{out} = I^2 \times R$. Between the artificial sea water and river water, PI-2DP membranes achieved an outstanding P_{out} of 48.4 W m^{-2} at 10^6 Ω when the current density equals 2 kA m^{-2}

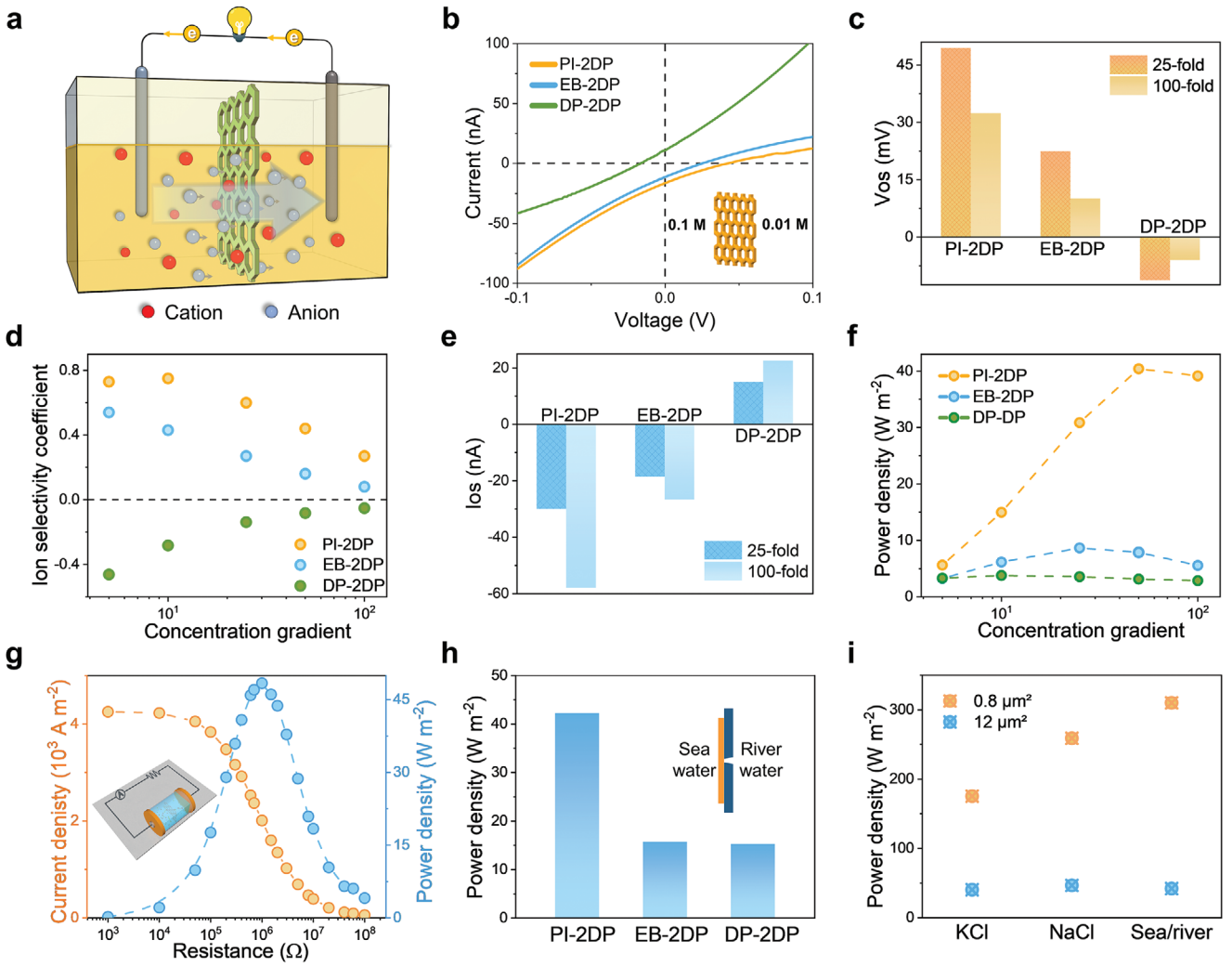

Figure 4. Osmotic energy conversion behavior. a) Schematic illustration of the osmotic energy conversion process. b) *I–V* curves of PI–, EB, and DP-2DP under 10-fold KCl concentration gradient. c) V_{os} of PI–, EB, and DP-2DP membranes measured under 25- and 100-fold KCl concentration gradient. d) Variations of ion selectivity coefficient in response to increasing KCl solution concentration gradient. e) I_{os} of PI–, EB, and DP-2DP membranes measured under 25- and 100-fold KCl concentration gradient. f) The power density calculated based on the measured I_{os} and V_{os} under different KCl concentration gradients. g) The current density and power output of PI-2DP membrane on the external circuit under a 50-fold NaCl concentration gradient. Inset: schematic of the experimental setup for measuring the osmotic power with an external load resistor. h) Power output of PI–, EB–, and DP-2DP membranes by mixing natural seawater and river water. i) Power density of PI-2DP membrane with various working areas.

(Figure 4g). The EB-2DP and DP-2DP can only achieve 15.4 and 1.2 W m^{-2} at 10^6 Ω with the current density of 1.1 and 0.3 kA m^{-2} (Figure S23, Supporting Information). We also measure the performance of PI-2DP membranes in long-term (Figure S24, Supporting Information). Under 10^6 Ω external resistance, the current density only declines 8% overall after 3 h with replenishment every hour. After 7 days, PI-2DP is capable of maintaining the P_{out} of 30 W m^{-2}. These results exhibit that the PI-2DP has considerable stability and robustness when applied in osmotic energy conversion. Furthermore, the natural seawater from Mediterranean Sea and river water from Elbe River were used to evaluate the practical osmotic energy conversion (Figure S25, Supporting Information). P_{out} of 42.2 W m^{-2} is obtained by PI-2DP, nearly three times the 15 W m^{-2} of EB– and DP-2DP (Figure 4h). The superior P_{out} values of PI-2DP certify the enhanced effect of dual-layer charge in ion selectivity compared to the contrasting 2DPs. When the testing area is reduced to sub-micrometre scale (<1 μm^2), PI-2DP achieves an exceptionally high P_{out} of 259 and 310 W m^{-2} in artificial and natural seawater and river water, respectively (Figure 4i). The outstanding performance in the sub-microscale device can be ascribed to the lower penetrating resistance, fewer grain boundaries, and fewer stochastic defects in the 2DP membranes.[22] Such a high power output outperforms the traditional ion-exchange membranes and the reported nanofluidic membranes, and is even double the value of the state-of-the-art 2DP and 2D COF membranes (≈135 W m^{-2} in artificial seawater and river water, Table S3, Supporting Information).[36] The outstanding performance of the PI-2DP in experiments agrees well with our theoretical designs, confirming that enhancement is achieved by the synergistic effect between the surface charge

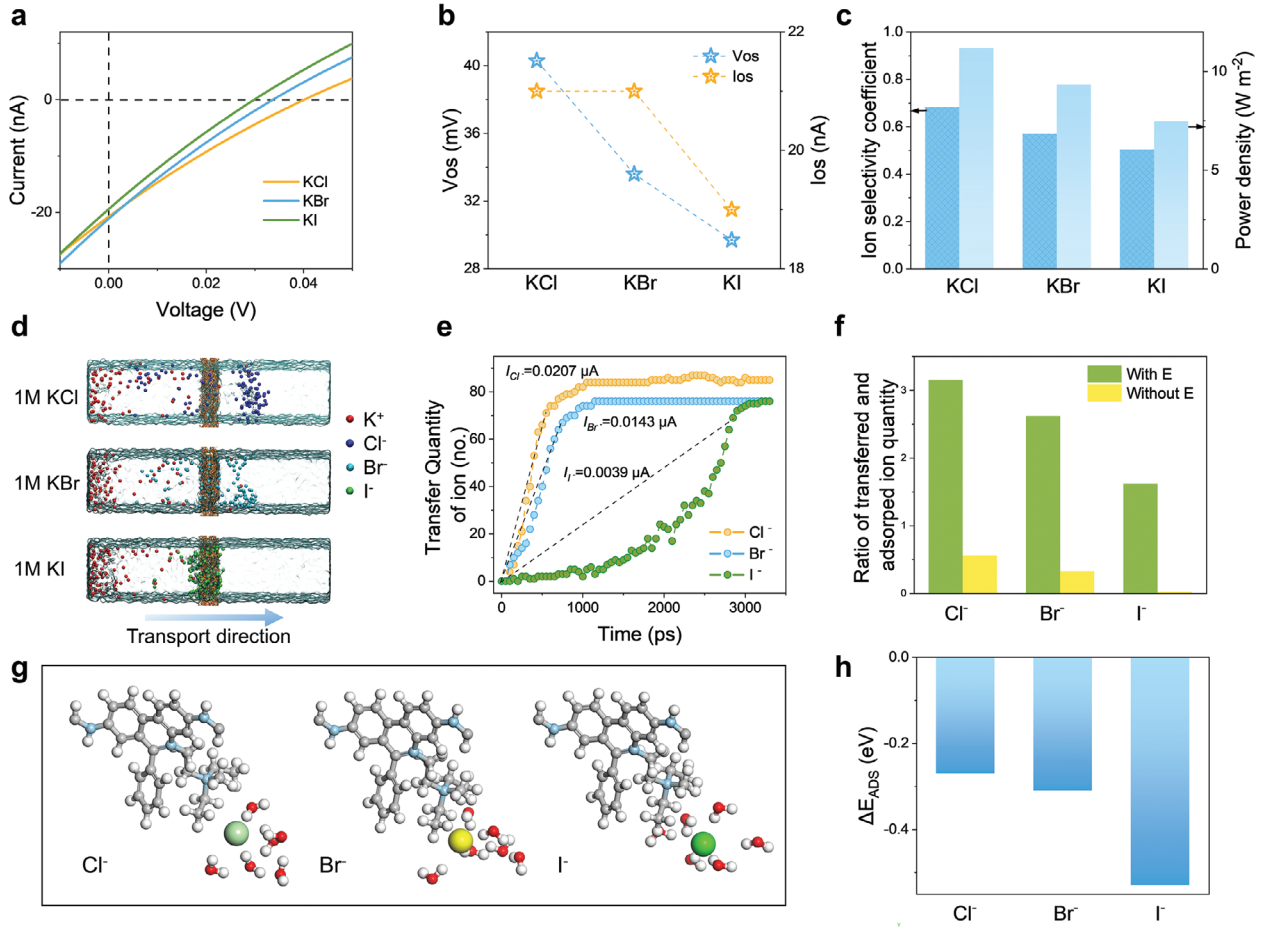

Figure 5. Anion transport mechanism. a–c) *I–V* curves (a), recorded V_{os} and I_{os} (b), and calculated ion selectivity coefficient and power density (c) of PI-2DP membranes measured under a 10-fold concentration gradient of KCl, KBr, or KI solutions, respectively. d) MD simulations of halide ions diffusion through the PI-2DP membranes in 1 M KCl, KBr, or KI solutions, respectively. e) Transfer quantity of Cl^-, Br^-, and I^- ions transport across PI-2DP membranes as a function of simulation time. f) The ratio of transferred and adsorbed ion quantity of Cl^-, Br^-, and I^- ions when diffusing through the PI-2DP membrane with and without electric field. g–h) DFT calculation model (g) and adsorption energy (h) of hydrated halide ions adsorbed to the positively charged sites of the PI-2DP.

and spatially aligned charge inside the well-defined PI-2DP channel.

2.5. Anion Transport Mechanism

The selective anion diffusion process under a concentration gradient was also investigated using varied potassium halide electrolytes including KCl, KBr, and KI (**Figure 5a**). Similar to Cl^- ion, the PI-2DP membrane also shows preferential selectivity toward Br^- and I^- ion, but with lower selectivity and ionic flux, evidenced by the lower V_{os} and I_{os} recorded in Figure 5b. The calculated ion selectivity coefficients in Figure 5c follow the order of Cl^- (0.68) > Br^- (0.57) > I^- (0.50). Accordingly, the power density of the KCl system is about 11.2 W m^{-2}, higher than that of KBr (9.3 W m^{-2}) and KI (7.5 W m^{-2}) when the concentration gradient is 10-fold. It is interesting that these three halide ions lead to different selective transport behavior although they have similar hydrated diameters and ion mobilities (Table S4, Supporting Information).[37]

Molecular dynamics (MD) is performed to provide insight into the adsorption interaction between the anions and inside channel of PI-2DPs. The initial simulation model is demonstrated in Figure S26 (Supporting Information).[38] The diffusion snapshots of halide electrolyte (1 M, KX, X = Cl^-, Br^- or I^-) at 800 ps are demonstrated in Figure 5d, in which the transport flux across the membranes follows the order of Cl^- > Br^- > I^-. Observed from Figure 5e and Figure S27 (Supporting Information), the transfer quantity of Cl^- is always the highest among the anions until they are stable, suggesting the preferable transport of Cl^- ions. In contrast, there is a very obvious gap in the transfer quantity between I^- and the other two (i.e., Cl^- and Br^-) that can be ascribed to their different electrostatic interaction with the channel wall.[38] This phenomenon implies that I^- ions encounter more friction inside the channel and thus their much slower diffusion behavior. The corresponding ionic currents, calculated as the product of the slope values for the linear regions of charge transfer–time curves and the elementary charge, follow the order of Cl^- (0.0207 μA) > Br^- (0.0143 μA) > I^- (0.0039 μA), consistent with the experimental trend in Figure 5b. Limited by the simulation size, the

transfer quantity of each anion would reach the maximum in 3000 ps. At that time, not all anions passed through the polymer framework, since they were adsorbed on it due to electrostatic interaction. The calculated ratio of transferred and adsorbed ion quantity based on Figure S22 (Supporting Information) also follows the same order (Figure 5f), and the results are more pronounced in the case of applying external driven force (i.e., electric field), in which Cl^- (3.15) > Br^- (2.62) > I^- (1.62).

DFT simulations are further performed to understand the interaction of anions with the 2DP frameworks.[22,39] As illustrated in the optimized binding structure in Figure 5g, the number of H_2O absorbed between the halide ion and N^+ increases from Cl^- to I^-, indicating the stronger interaction between the N^+ in the quaternary ammonium group and the halide ion. Specifically, the N^+ acts as an effective site, which makes the H in the methyl group positively charged. Then the H attracts the oxygen in the hydration layer of the halide ion, which pulls the halide ion close to the positively charged skeleton of 2DP. The corresponding adsorption energies, $E_{adsorption}$, are all negative values, representing the preferential attraction between the halide ion and PI-2DP framework (Figure 5g), with the values following the order of I^- (−0.53 eV) > Br^- (−0.31 eV) > Cl^- (−0.27 eV) (Figure 5h). Since stronger adsorption results in a larger energy barrier, the anion diffusion through PI-2DP membrane follows a reverse order. The highest $E_{adsorption}$ of I^- causes a tight binding to the N^+ site in the polymer skeleton, which corresponds to its slow velocity through the membrane in MD simulations.

3. Conclusion

In summary, giant blue energy is harvested by novel PI-2DP membranes with well-defined pore channels and dual electrostatic effect. The fully crystalline PI-2DP exhibits charge governed ion transport behavior, and achieves superior anion selectivity among wide pH and concentration ranges than the contrast EB-2DP with only skeleton charges. A great power density of 48.4 W m^{-2} is achieved when mixing artificial seawater and river water in the sub-microscale device, outperforming the traditional ion-exchange membranes and most reported nanofluidic membranes. The outstanding power output is attributed to the high density of well-defined cationic sites, and the synergistic coupling effect between the inherent spatially aligned and skeleton charges, enabling low-energy-barrier transport. The realization of this dual-layer charge distribution within the 2DP membranes sheds light on the design principles for achieving low-energy-barrier nanoscale confinements, the future works including upscaling the membrane preparation, and integrating them into practical reverse electrodialysis setup are also needed. This work has significant implications for various applications such as nanofiltration, electrodialysis, and water desalination, considering the key role played by ion transporting membranes in these areas.

4. Experimental Section

Materials: Propidium iodide, ethidium bromide, and 3,8-diamino-6-phenylphenanthridin were purchased from Sigma–Aldrich. Sodium *n*-octyl sulfate was purchased from abcr. 2,4,6-Triformylphloroglucinol was purchased from Fluorochem. Sodium dodecyl sulfate was purchased from TCI.

Numerical Simulation: Based on the 2D Poisson–Nernst–Planck (PNP) model, the theoretical simulation was conducted by using COMSOL Multiphysics.[20,40–43] Three models were constructed to simulate three types of inherent nanochannels: model (i) simulates the nanochannel that has one charged layer of 1.2 nm diameter; model (ii) simulates the nanochannel that has one charged layer of 1.8 nm diameter; model (iii) simulates the nanochannel which has both inner (d = 1.2 nm) and out (d = 1.8 nm) charged layers. The channel length of all three models is 36 nm. Two electrolyte reservoirs were introduced in order to decrease the effect of entrance/exit mass transfer resistances on the overall transport of ions. The surface charge density of all charged wall is uniformly set to 3.45 mC m^{-2}. The coupled PNP equations can be solved utilizing appropriate boundary conditions and generate anion concentration profiles, potential and ion flux through the nanochannel. The Nernst–Planck Equation (1) is able to describe the ion transport properties of a charged nanochannel:

$$j_i = D(\nabla c_i + \frac{z_i F c_i}{RT}\nabla\varphi) + c_i u \tag{1}$$

where j_i, D_i, c_i, and z_i are the ionic flux, diffusion coefficient, ion concentration, and valence number for each ion species i; φ and ϵ are electrical potential and dielectric constant, respectively; F, R, T, and u are the Faraday constant, universal gas constant, absolute temperature, and fluid velocity, respectively.

The Poisson Equation (2) can describe the relationship between electrical potential and ion concentration:

$$\nabla^2\varphi = -\frac{\rho_e}{\epsilon_0\epsilon_r} \tag{2}$$

where ϵ_0, ϵ_r are the permittivity of free space and the relative permittivity of the medium. The space charge density (ρ_e) is given as Equation (3). The ion flux j_i for each ion should satisfy the continuity Equation (4) when the system reaches stationary regime:

$$\rho_e = F\sum_{k=1}^{m} z_i c_i \tag{3}$$

$$\nabla \cdot J_i = 0 \tag{4}$$

where m is the number of ionic species. The boundary condition for potential φ on the channel wall is:

$$n \cdot \nabla\varphi = -\frac{\sigma}{\epsilon_0\epsilon_r} \tag{5}$$

where σ is the surface charge density. Impermeable boundary conditions are applied at both entrances for ionic concentration and electric field. The ionic flux has the zero normal components at boundaries:

$$n \cdot j_i = 0 \tag{6}$$

The ion transport property inside the nanochannel can be known by solving the coupled Equations (1)–(4) with boundary conditions (5)–(6).

Synthesis of PI-2DP Membranes: Polycrystalline PI-2DP membranes were synthesized by the surfactant monolayer assisted interfacial synthesis (SMAIS) method. First, at room temperature, 50 mL of deionized water was injected into a cleaned glass dish with a diameter of 50 mm and a height of 60 mm. After the static air–water interface formed, 20 µL sodium *n*-octadecyl sulfate (0.086 µmol in mixture of methanal, hexane, and chloroform) was carefully spread onto the interface dropwise by syringe. Then the dish was transferred into the 50 °C oven steadily to keep the surface static. After 1 h for the evaporation of surfactant solvent, monomer 1 (M1) (2.24 µmol propidium bromide in 0.5 mL 5.7 mmol mL^{-1} CF_3SO_3H)

was slowly injected into the water subphase by pipetting gun. After another 1 h for the dispersion of M1, monomer 2 (M2) (0.014 mmol 2,4,6-triformylphloroglucinol in 3 mL water) was injected into the solution by syringe successively. This reaction was kept at 50 °C without disturbance for 2 days. Then the continuous membrane with orange colour was formed on the water–air surface by the polycondensation between M1 and M2. The PI-2DP membrane was fished out by Si wafer and cleaned with water to remove the surfactant and ligands. Then the membrane was deposited on different substrates and dried at 80 °C for 1 h.

General Characterization: Optical microscopy (Zeiss), AFM (Bruker, USA), scanning electron microscopy (SEM, Zeiss Gemini 500), transmission electron microscopy (TEM, Zeiss Libra 200KV), and GIWAXS were used to investigate the morphology and structure of the PI–, EB–, and DP-2DP membranes. FTIR (SHIMADZU, QATR-S) and surface-enhanced Raman spectra were used to characterize the formation of the 2DP membranes.

For the GIWAXS measurements the 2DP membranes were transferred onto Si wafer. The measurements of PI-2DP and EB-2DP were performed at the BL11 – NCD-SWEET beamline at ALBA Synchrotron, Spain. The X-ray beam energy was set to 12.4 keV and the beam size was 50 µm (vertically) and 130 µm (horizontally). The angle of incidence was 0.12° and the samples were exposed to the beam for 30 s. The scattering patterns were recorded using a Rayonix LX255-HS area detector and the average of four images was used for analysis. The detector was positioned about 170 mm behind the sample and Cr_2O_3 was used to calibrate the sample–detector distance and the position of the beam on the detector. The measurement of DP-2DP was performed at the SIRIUS beamline at SOLEIL, France. Here, the beam energy was 12 keV and the beam had dimensions of 70 µm vertically and 500 µm horizontally. The incidence angle was 0.1° and a Dectris Pilatus 1 M area detector was used for recording the images. The sample–detector distance was 380 mm and a silver behenate reference was used to verify the distance and direct beam position on the detector. The sample was then exposed to the beam for 5 × 30 s and the final image was then an average of the five recorded images. Data visualization and analysis was performed with the software package WxDiff.

Electrical Measurements: After fished out and washed with water, three layers of 2DP membranes were deposited on a silicon wafer with a conical hole (area of the small side is 12 μm^2) in the center, and the small side of the hole was covered with 2DP membranes. Then the Si wafer was sandwiched between two chambers tightly (Figure S12, Supporting Information). Standard electrodes (saturated Ag/AgCl salt bridge electrodes, HANA Instruments) were used to record the voltage and current signals.[44] KCl electrolyte solution was selected as the standard electrolyte owing to the similar diffusion coefficients of K^+ and Cl^- ions (about 1.96×10^{-9} and 2.03×10^{-9} m^2 s^{-1}).[14] An amount of 0.5 and 0.01 M NaCl electrolyte solutions were chosen as artificial seawater and river water. All the testing solutions except natural seawater and river water were prepared by mixing deionized water and pure salts. The salinity of natural sea water and river water is 0.4 M and 0.003 M NaCl that is obtained by ionic conductivity measurement. A standard conductivities-concentration curve is plotted by measuring a series of standard NaCl electrolytes with known concentrations. Then, the conductivities of the natural seawater and natural river water were measured, which were 36 500 and 442 µs cm^{-1}, respectively. The corresponding salt concentrations were calibrated with the standard curve. During the measurements, the KCl electrolyte solutions were adjusted to the expected pH and then injected slightly into each compartment by dropper. The pH tester (Orion Star) was used to confirm the pH value of the solutions. The linear sweep voltammetry (LSV) and amperometric *i–t* curve measurements were carried out with an electrochemical workstation (CHI).

Ionic Conductance Model: When there was no concentration gradient applied on the two sides of 2DP membrane, the ionic conductance was obtained. The ionic conductance G of a nanofluidic channel, which is the sum of bulk conductance G_{bulk} dominates in high concentration and surface conductance $G_{surface}$ dominates in low concentration:

$$G = G_{bulk} + G_{surface} = q(\mu_{K+} + \mu_{Cl-})C_B N_A wh/l + 2\mu_{Cl-}\sigma_s h/l \quad (7)$$

where q is the elementary charge (1.6×10^{-19} C). μ_{K+} and μ_{Cl-} are the mobility of K^+ (7.6×10^{-8} m^2 s^{-1} v^{-2}) and Cl^- (7.9×10^{-8} m^2 s^{-1} v^{-2}), respectively; C_B is the bulk solution concentration; N_A is Avogadro's number; Here, w and l are the dimensions of the unit pore of about 2.42 nm. l is 2DP membrane thickness for conductance measurement of about 45 nm; σ_s is the surface charge density.

When C_B is 1 M, G is assumed to equal to G_{bulk}. Since G is the conductance per channel, the channel number can be calculated from the ratio between the experimental value and G_{bulk} at 1 M. Then the experimental values of conductance were obtained under different KCl concentrations, and were fitted by variable surface charge density model as shown in Figure 3c. Meanwhile, the conductance values depending on constant surface charge density (3.45 mC m^{-2}) were also plotted as the orange dash line. Through the same approach, we calculated the surface charge density of EB– and DP-2DP which are 1.93 and −1.4 mC m^{-2}, respectively.

Ion Selectivity Coefficient: Ion selectivity coefficient S is a parameter for evaluating the ion-selective ability of the membranes. For anion-selective membranes, the value of S ranges from 0 to 1, in which 0 represents non-selective case and 1 represents the ideal anion-selectivity. S is calculated by:

$$S = \frac{V_{os}F}{RT \ln \frac{C_{high}}{C_{low}}} \quad (8)$$

where V_{os} is the osmotic potential recorded from the *I–V* curve under concentration gradient; F is Faraday constant; R is universal gas constant; T is the absolute temperature. C_{high} and C_{low} are the concentration of the concentrated side and diluted side of the 2DP membranes, separately.

Molecular Dynamic Simulations: For the simulations with electric filed, a triclinic box with $a = 5.1$ nm, $b = 5.24$ nm, $c = 21.6$ nm, $\alpha = 90°$, $\beta = 90°$, and $\theta = 62.4°$ was used. The structure of PI-2DP was obtained from DFT calculation. Two stacked layers of PI-2DP were placed in the middle of the simulation box and perpendicular to the *c*-axis,and only side chains are allowed to move (Figure S21, Supporting Information). An 1 M KX solutions was placed in one side of PI-2DP where X^- represents Cl^-, Br^-, and I^-, and pure water was placed in the other side. Since PI-2DP was positively charged, additional X^- ions were added to neutralize the system. The density of the solutions was determined by experiments. The packing of water molecules and ions was performed using Packmol software.[45] Parameters of the atomistic models of PI-2DP were based on the GAFF force field.[46] The parameters of Cl^-, Br^-, and I^- were obtained from the literature.[47] For water molecules, the OPC model was used.[48] Periodic boundary conditions were performed in *xy* plane. Temperature coupling was performed using a v-rescale thermostat.[49] Prior to the dynamics simulation, the steepest descent algorithm was used to pre-equalize the system for eliminating the excessive stress in initial structures.[50] After pre-equilibrium, an NVT ensemble without electric field was used to equilibrate the system under room conditions (298.15 K) for 100 ps. Then, a 10 ns production simulation in the NVT ensemble at 298.15 K was carried out for ion transport simulation under 1 V nm^{-1} electric field along *c*-axis. For the simulations without electric field, two vacuum layers with thickness of 10 nm were introduced at both ends of the *c*-axis and 3D periodic boundary conditions were adopted. The steepest descent algorithm was used to pre-equalize the system. Then, a 10 ns production simulation in the NVT ensemble at 298.15 K was carried out for ion transport simulation. All simulations were performed via GROMACS 2019.4 software package.[51] All visualization structures were provided by VMD 1.9.3 software.[52]

DFT Calculation Details: The first-principles calculations were carried out with the Vienna ab initio simulation package (VASP).[53,54] The interaction between ions and valence electrons was described using projector augmented wave (PAW) potentials, and the exchange-correlation between electrons was treated through using the generalized gradient approximation (GGA) in the Perdew–Burke–Ernzerhof (PBE) form.[55] DFT-D3 method was employed to calculate the van der Waals (vdW) interaction.[56] To achieve the accurate simulations, the plane wave cutoff energy was 450 eV, a Gamma centered k-point grid of 1 × 1 × 3 was used for bulk

models. Ionic relaxations were carried out under the conventional energy (10^{-4} eV) and force (0.03 eV $Å^{-1}$) convergence criteria.

For adsorption energy calculations of different anions on PI-2DP models, two-layer slab models of 2DP were constructed as the substrate, in which 15 Å vacuum layer along *z* direction was applied to avoid the interaction of anions. A single Gamma centered k-point grid was performed for the calculations of slab models. One anion (Cl^-, Br^-, and I^-) and six water molecules were used to simulate the hydrated anions in the solution. Adsorption energies $E_{adsorption}$ were given with reference to the isolated surface $E_{surface}$ relaxed upon removing the molecule from the unit cell using identical computational parameters and the energy of the molecule $E_{molecule}$ as following:

$$E_{adsorption} = E_{moleculeonsurface} - E_{surface} - E_{molecule} \quad (9)$$

Supporting Information

Supporting Information is available from the Wiley Online Library or from the author.

Acknowledgements

This work was financially supported by the European Union's Horizon 2020 research and innovation programme under grant agreement No 881603, the European Science Foundation (ESF), Coordination Networks: Building Blocks for Functional Systems (SPP1928, COORNET), CRC1415, ERC Grants on T2DCP and FC2DMOF (No.852909), and Leading Talents of Innovation and Entrepreneurship of Gusu District (SJ202300012023). The research leading to this result has been supported by the project CALIP-SO plus under Grant Agreement 730872 from the EU Framework Programme for Research and Innovation HORIZON 2020. Parts of these experiments were performed at BL-11-NCD-SWEET beamline at ALBA Synchrotron with the collaboration of ALBA staff. The authors would like to thank Dr. Marc Malfois for help with setting up the experiment. The authors acknowledge SOLEIL for provision of synchrotron radiation facilities and would like to thank Dr. Arnaud Hemmerle for assistance in using beamline SIRIUS.

Open access funding enabled and organized by Projekt DEAL.

Conflict of Interest

The authors declare no conflict of interest.

Data Availability Statement

The data that support the findings of this study are available from the corresponding author upon reasonable request.

Keywords

2D polymer, ion transport, nanofluidics, osmotic energy conversion

Received: October 16, 2023
Revised: January 23, 2024
Published online:

[1] A. Siria, M.-L. Bocquet, L. Bocquet, *Nat. Rev. Chem.* **2017**, *1*, 0091.
[2] A. Zlotorowicz, R. V. Strand, O. S. Burheim, Ø. Wilhelmsen, S. Kjelstrup, *J. Membr. Sci.* **2017**, *523*, 402.
[3] Z. Fang, Y. Dong, Z. Guo, Z. Zhao, Z. Zhang, Z. Liang, H. Yao, *Appl. Phys. A* **2022**, *128*, 1080.
[4] C. Li, L. Wen, X. Sui, Y. Cheng, L. Gao, L. Jiang, *Sci. Adv.* **2021**, *7*, eabg2183.
[5] Y. Mei, C. Y. Tang, *Desalination* **2018**, *425*, 156.
[6] J. G. Hong, B. Zhang, S. Glabman, N. Uzal, X. Dou, H. Zhang, X. Wei, Y. Chen, *J. Membr. Sci.* **2015**, *486*, 71.
[7] Y.-C. Liu, L.-H. Yeh, M.-J. Zheng, K. C. W. Wu, *Sci. Adv.* **2021**, *7*, eabe9924.
[8] A. Siria, P. Poncharal, A.-L. Biance, R. Fulcrand, X. Blase, S. T. Purcell, L. Bocquet, *Nature* **2013**, *494*, 455.
[9] J. Feng, M. Graf, K. Liu, D. Ovchinnikov, D. Dumcenco, M. Heiranian, V. Nandigana, N. R. Aluru, A. Kis, A. Radenovic, *Nature* **2016**, *536*, 197.
[10] L. Wang, M. S. H. Boutilier, P. R. Kidambi, D. Jang, N. G. Hadjiconstantinou, R. Karnik, *Nat. Nanotechnol.* **2017**, *12*, 509.
[11] K. Raidongia, J. Huang, *J. Am. Chem. Soc.* **2012**, *134*, 16528.
[12] A. R. Koltonow, J. Huang, *Science* **2016**, *351*, 1395.
[13] M. Macha, S. Marion, V. V. R. Nandigana, A. Radenovic, *Nat. Rev. Mater.* **2019**, *4*, 588.
[14] S. Hong, F. Ming, Y. Shi, R. Li, I. S. Kim, C. Y. Tang, H. N. Alshareef, P. Wang, *ACS Nano* **2019**, *13*, 8917.
[15] Z. Zhang, S. Yang, P. Zhang, J. Zhang, G. Chen, X. Feng, *Nat. Commun.* **2019**, *10*, 2920.
[16] C. Cheng, G. Jiang, G. P. Simon, J. Z. Liu, D. Li, *Nat. Nanotechnol.* **2018**, *13*, 685.
[17] H. Zhan, Z. Xiong, C. Cheng, Q. Liang, J. Z. Liu, D. Li, *Adv. Mater.* **2020**, *32*, 1904562.
[18] W. Xin, L. Jiang, L. Wen, *Acc. Chem. Res.* **2021**, *54*, 4154.
[19] C. Cheng, G. Jiang, C. J. Garvey, Y. Wang, G. P. Simon, J. Z. Liu, D. Li, *Sci. Adv.* **2016**, *2*, e1501272.
[20] H. S. White, A. Bund, *Langmuir* **2008**, *24*, 2212.
[21] Z. Wang, Z. Zhang, H. Qi, A. Ortega-Guerrero, L. Wang, K. Xu, M. Wang, S. Park, F. Hennersdorf, A. Dianat, A. Croy, H. Komber, G. Cuniberti, J. J. Weigand, U. Kaiser, R. Dong, X. Feng, *Nat. Synth.* **2022**, *1*, 69.
[22] Z. Zhang, P. Bhauriyal, H. Sahabudeen, Z. Wang, X. Liu, M. Hambsch, S. C. B. Mannsfeld, R. Dong, T. Heine, X. Feng, *Nat. Commun.* **2022**, *13*, 3935.
[23] Z. S. Siwy, S. Howorka, *Chem. Soc. Rev.* **2010**, *39*, 1115.
[24] X. Hou, *Adv. Mater.* **2016**, *28*, 7049.
[25] C. H. Duan, A. Majumdar, *Nat. Nanotechnol.* **2010**, *5*, 848.
[26] S. Hong, C. Constans, M. V. Surmani Martins, Y. C. Seow, J. A. Guevara Carrió, S. Garaj, *Nano Lett.* **2017**, *17*, 728.
[27] Z. Zhang, P. Zhang, S. Yang, T. Zhang, M. Löffler, H. Shi, M. R. Lohe, X. Feng, *Proc. Natl. Acad. Sci. U. S. A.* **2020**, *117*, 13959.
[28] S. Qin, D. Liu, G. Wang, D. Portehault, C. J. Garvey, Y. Gogotsi, W. Lei, Y. Chen, *J. Am. Chem. Soc.* **2017**, *139*, 6314.
[29] J.-J. Shao, K. Raidongia, A. R. Koltonow, J. Huang, *Nat. Commun.* **2015**, *6*, 7602.
[30] I. Vlassiouk, Z. S. Siwy, *Nano Lett.* **2007**, *7*, 552.
[31] M. A. Brown, A. Goel, Z. Abbas, *Angew. Chem., Int. Ed.* **2016**, *55*, 3790.
[32] M. Caglar, I. Silkina, B. T. Brown, A. L. Thorneywork, O. J. Burton, V. Babenko, S. M. Gilbert, A. Zettl, S. Hofmann, U. F. Keyser, *ACS Nano* **2020**, *14*, 2729.
[33] R. H. Tunuguntla, R. Y. Henley, Y.-C. Yao, T. A. Pham, M. Wanunu, A. Noy, *Science* **2017**, *357*, 792.
[34] J. Lu, H. Zhang, J. Hou, X. Li, X. Hu, Y. Hu, C. D. Easton, Q. Li, C. Sun, A. W. Thornton, M. R. Hill, X. Zhang, G. Jiang, J. Z. Liu, A. J. Hill, B. D. Freeman, L. Jiang, H. Wang, *Nat. Mater.* **2020**, *19*, 767.
[35] A. Esfandiar, B. Radha, F. C. Wang, Q. Yang, S. Hu, S. Garaj, R. R. Nair, A. K. Geim, K. Gopinadhan, *Science* **2017**, *358*, 511.
[36] J. Yang, B. Tu, G. Zhang, P. Liu, K. Hu, J. Wang, Z. Yan, Z. Huang, M. Fang, J. Hou, Q. Fang, X. Qiu, L. Li, Z. Tang, *Nat. Nanotechnol.* **2022**, *17*, 622.

[37] X. Li, H. Zhang, P. Wang, J. Hou, J. Lu, C. D. Easton, X. Zhang, M. R. Hill, A. W. Thornton, J. Z. Liu, B. D. Freeman, A. J. Hill, L. Jiang, H. Wang, *Nat. Commun.* **2019**, *10*, 2490.
[38] Z. Man, J. Safaei, Z. Zhang, Y. Wang, D. Zhou, P. Li, X. Zhang, L. Jiang, G. Wang, *J. Am. Chem. Soc.* **2021**, *143*, 16206.
[39] L. Cao, I. C. Chen, X. Liu, Z. Li, Z. Zhou, Z. Lai, *ACS Nano* **2022**, *16*, 18910.
[40] X. F. Zhang, X. Zhang, Z. G. Qu, J. Q. Pu, Q. Wang, *Appl. Energy* **2022**, *326*, 120005.
[41] L. Ma, Z. Li, Z. Yuan, H. Wang, C. Huang, Y. Qiu, *J. Power Sources* **2021**, *492*, 229637.
[42] X. Zhang, Z. Qu, Q. Wang, M. Iqbal, *Energy Convers. Manage.* **2022**, *273*, 116373.
[43] W. Xian, X. Zuo, C. Zhu, Q. Guo, Q.-W. Meng, X. Zhu, S. Wang, S. Ma, Q. Sun, *Nat. Commun.* **2022**, *13*, 3386.
[44] S. Garaj, W. Hubbard, A. Reina, J. Kong, D. Branton, J. A. Golovchenko, *Nature* **2010**, *467*, 190.
[45] M. C. Payne, M. P. Teter, D. C. Allan, T. A. Arias, J. D. Joannopoulos, *Rev. Mod. Phys.* **1992**, *64*, 1045.
[46] J. Wang, R. M. Wolf, J. W. Caldwell, P. A. Kollman, D. A. Case, *J. Comput. Chem.* **2004**, *25*, 1157.
[47] A. Sengupta, Z. Li, L. F. Song, P. Li, K. M. Merz Jr., *J. Chem. Inf. Model.* **2021**, *61*, 869.
[48] S. Izadi, R. Anandakrishnan, A. V. Onufriev, *J. Phys. Chem. Lett.* **2014**, *5*, 3863.
[49] H. J. C. Berendsen, J. P. M. Postma, W. F. van Gunsteren, A. DiNola, J. R. Haak, *J. Chem. Phys.* **1984**, *81*, 3684.
[50] G. Bussi, D. Donadio, M. Parrinello, *J. Chem. Phys.* **2007**, *126*, 014101.
[51] M. J. Abraham, T. Murtola, R. Schulz, S. Páll, J. C. Smith, B. Hess, E. Lindahl, *SoftwareX* **2015**, *1–2*, 19.
[52] H. William, D. Andrew, S. Klaus, *J. Mol. Graphics* **1996**, *14*, 33.
[53] G. Kresse, J. Furthmüller, *Comput. Mater. Sci.* **1996**, *6*, 15.
[54] Y. Surendranath, M. W. Kanan, D. G. Nocera, *J. Am. Chem. Soc.* **2010**, *132*, 16501.
[55] J. P. Perdew, K. Burke, M. Ernzerhof, *Phys. Rev. Lett.* **1996**, *77*, 3865.
[56] S. Grimme, J. Antony, S. Ehrlich, H. Krieg, *J. Chem. Phys.* **2010**, *132*, 154104.